Check for updates

Received: 17 September 2023 | Revised: 20 February 2024 | Accepted: 27 February 2024

DOI: 10.1002/esp.5817

RESEARCH ARTICLE

ESPL WILEY

Modelling the impact of a dam-break wave on a vertical wall

Andrea Del Gaudio[1] | Giovanni La Forgia[2,3] | George Constantinescu[4] | Francesco De Paola[1] | Cristiana Di Cristo[1] | Michele Iervolino[5] | Angelo Leopardi[2] | Andrea Vacca[1]

[1]DICEA, University of Naples Federico II, Napoli, Italy

[2]DICeM, University of Cassino and Southern Lazio, Cassino, Italy

[3]Institute of Marine Sciences, National Research Council of Italy (ISMAR-CNR), Rome, Italy

[4]Department of Civil and Environmental Engineering and IIHR -Hydroscience and Engineering, University of Iowa, Iowa City, Iowa, USA

[5]DI, University of Campania Luigi Vanvitelli, Aversa, Italy

Correspondence
Andrea Del Gaudio, DICEA, University of Naples "Federico II", Napoli, 80125, Italy.
Email: andrea.delgaudio@unina.it

Summary

Dam-Break waves arise from the sudden release of the water stored behind a wall, and they cause destruction and losses on nearby areas. Characterisation of the impact force on obstacles is very important for risk assessment. In this work, we performed a series of lock-release experiments to evaluate the wave-induced impact force on a vertical end wall situated some distance from the lock. Laboratory data were used to evaluate the performance of several types of numerical models to predict the wave-induced force on the vertical end wall. The selected models were as follows: the hydrostatic 1D De Saint-Venant model, the multi-layer hydrostatic model and the Navier–Stokes two-phase flow. For the latter two models, both 2D (in the *x-z* plane) and 3D simulations were performed. The results show that, independently of the hydrostatic assumption, the 2-D simulations generate nonphysical oscillations which are not present in the measured temporal histories of the pressure and force values. By contrast, the predictions of both 3D numerical models better reproduce the temporal variation of the pressure forces on the end wall. The present study also shows that from a practical point of view, the 1D De Saint-Venant model predicts with sufficient accuracy the impact time and the magnitude of the peak value of the impact force. Therefore, if the use of a fully 3D models is not a feasible option, in terms of a trade-off between computation cost and accuracy, the use of a simple hydrostatic 1D De Saint-Venant model is preferable to a 2D model.

KEYWORDS
dam-break, experiments, impact force, numerical simulation, unsteady flows

1 | INTRODUCTION

Dam-break waves arise from the sudden release of water stored behind a wall and may cause human fatalities, ecological and environmental hazard, damages and huge economic losses to the surrounding landscape (Wúthrich et al., 2019). These waves are defined as surges, whether they develop over a dry bed, or bores, if they propagate over a wet bed. Tsunamis, tidal bores and the collapse of an artificial embankment may also lead to similar unsteady flows. For instance, Chanson (2009) stated that a tsunami surge that propagates on a coastal plain behaves as a dam-break wave. Indeed, in both cases, the wavefront is a shock front for both flow depth and velocity (Chanson, 2009). Additionally, during their propagation, these waves may encounter obstacles, and the evaluation of the impact dynamics and magnitude of the impact forces is of utmost interest for risk mitigation. Extreme precipitation and runoff induced by climate change may dramatically contribute to enhance flood risks and potential dam failures. The recent scientific interest in predicting consequences of dam-break events is consequently increased (Fluixá-Sanmartín et al.,2018).

Numerical modelling is nowadays an accessible and potentially useful tool to predict the dam-break wave propagation and its interaction with structures situated along its path. Numerical simulations allow evaluating the hydraulic characteristics relevant for flood hazard analysis, but they also provide the starting point for the evaluation of sediment transport, erosion/deposition patterns and for the study of water-biota-sediment interactions. Simulations also support the evaluation of impact forces acting against obstacles located along the path of the wave. Given the need to use numerical simulations for field-scale applications, it is important to identify the most suitable

 © 2024 John Wiley & Sons Ltd.

tool among the different available approaches, considering both accuracy and computational costs. Therefore, the comparison of numerical results with measured data is crucial to assess the performance of the mathematical models. Both Chanson (2009) and Aureli et al. (2023) have highlighted that apart from few exceptions (e.g. Aureli et al., 2015), detailed experimental data to fully assess the predictive capabilities of such models are not widely available, although such data are of utmost importance for numerical models validation (Aureli et al., 2015; Fang et al., 2022; Lara et al., 2012; Robertson et al., 2013; Stamataki et al., 2018; Wang et al., 2022; Wüthrich et al., 2018; Wúthrich et al.2019).

Literature rarely reports in-field measurements of these flows, since during their occurrence data collection or visual observations are very difficult to perform (Wúthrich et al., 2019). Available data are often obtained from postforensic engineering reconstructions of the event. The scarcity of field observations, on which policymakers can base and develop safety procedures (Lynett, 2022), suggests the use of laboratory experiments to gain insights and obtain the critical engineering information to assess risk and to develop a mitigation plan. Concerning the dynamic interaction between unsteady flows and obstacles, Ramsden (1996) presented a pioneering experimental study on surges and bores impacting against a vertical wall. He analysed the time history of the dam-break wave run-up and measured the induced impact force and pressure at a point on the wall. As the water level reached its maximum elevation on the vertical wall, the study found that the force and the momentum, estimated by assuming hydrostatic pressure distribution, exceeded the maximum measured values. Since this seminal contribution, several experimental studies in the last two decades focused on the interaction between water waves and obstacles, investigating the hydrodynamics and the resulting impact pressures (Arnason, 2005; Bidoae et al.2003; Kleefsman et al., 2005; Nistor et al., 2009; Oertel & Bung, 2012). Later on, Lobovsk et al. (2014) investigated the repeatability and three-dimensional effects associated with the impact dynamics of a dam-break wave against a vertical wall. Although their analysis was limited to a single initial water height, they provided the first data set of experimental images and local pressure measurements on the wall. Moreover, they showed that three-dimensional effects appeared during the impacting phase. They found that the maximum pressure peak sampled by the pressure transducers was significantly larger for the centred sensor than for the displaced one. More recently, Shen et al. (2020), Liu et al. (2022) and Xie and Shimozono (2022) investigated a similar experimental layout. Interestingly, Liu et al. (2022) showed that the horizontal dynamic pressure peaked when the wave run-up height was at its minimum level. As the surge started falling off the wall and breaking at its base, the magnitude of the dynamic pressure was close to that of the hydrostatic pressure. Their study also highlighted three-dimensionality effects induced by the side walls that slightly delayed and decreased the impact pressure sampled by the lateral transducers compared with those situated near the wall centreline. Tan et al. (2023) quantitatively investigated the flow kinematics and turbulence characteristics of the dam-break flow impacting against a vertical wall. They found that during the impact phase following the dam-break, two counterclockwise vortexes were generated, the first one generated by the main body of water and the smaller one forming in the wall-bed junction region.

An accurate representation of the complex interaction between a highly unsteady turbulent flow, that is, the water wave, with an obstacle, requires an advanced numerical model, ideally a three-dimensional (3D) model using the Large Eddy Simulation (LES) approach. At the same time, the need to employ numerical simulations for field-scale predictions pushes towards the reduction of the model complexity which translates into a significant reduction of the overall computational cost. In this regard, the comparison among different modelling alternatives should take into account three aspects: (i) the kinematic interaction with the channel sidewalls, (ii) turbulence effects and (iii) the assumption of hydrostatic pressure distribution. The discussion below is restricted only to Eulerian models, which are commonly used for such simulations.

In terms of their complexity, the depth-integrated models based on solving the one- dimensional (1D) or two-dimensional (2D) De Saint-Venant equations (Castro-Orgaz & Hager, 2019) (DSV) are the simplest ones. In DSV models, turbulent stresses are not further accounted for; the hydrostatic pressure distribution is assumed along the direction normal to the bottom, and the bottom shear stress is accounted for.

The DSV approach is widely used to model propagation of dam-break waves, even in the presence of obstacles, buildings (either isolated or multiple) and topographical singularities (Aureli et al., 2015; Brufau et al., 2002; Mingham & Causon, 1998; Lai et al., 2005; Ortiz, 2014; Soares Frazao & Zech, 2002). Such low-computational cost models allowed practitioners to make predictions for field-scale flood management applications.

Compared with the DSV approach, the Reynolds-averaged Navier–Stokes (RANS) and the LES approaches allow to relax the aforementioned assumptions especially when incorporated in a three-dimensional solver; namely, they estimate in a physically much more correct way the turbulent stresses and accurately account for non-hydrostatic pressure effects on the flow. The last issue is particularly relevant when dealing the dam-break wave impacts a bluff-body obstacle, in which case the flow develops strong curvature with non-negligible deviations from the hydrostatic pressure distribution (Aureli et al., 2015). In some cases, 3D LES models were successfully used to simulate the interaction of buoyancy driven flows with isolated and series of obstacles (Constantinescu, 2014; Gonzalez-Juez et al., 2010; La Forgia et al., 2018; Tokyay et al., 2011, 2012, 2014; Tokyay & Constantinescu, 2015). A main challenge when applying such models to dam-break flows is that the dynamics of the interface between the wave fluid and the air needs to be solved using a separate mode (Ai et al., 2022). One of the most used techniques for tracking the free surface in dam-break applications is the Volume of Fluid (VOF) method (Biscarini et al., 2010; Munoz & Constantinescu, 2020; Marsooli & Wu, 2014; Ozmen-Cagatay & Kocaman, 2011).

Examples of using this approach to simulate dam-break flows without obstacles placed along their path can be found in Garoosi et al. (2022) (2D and 3D RANS) and Larocque et al. (2013) (3D LES).

Several studies have compared the predictive abilities of DSV-, RANS- and LES-based models to predict the propagation of dam-break waves over surfaces without obstacles. For example, Ozmen-Cagatay and Kocaman (2011) compared the experimental results of the early stages of a dam-break wave on dry and wet bed, with simulations conducted with a RANS-VOF code using the $k-\epsilon$ turbulence model and with simulations obtained using a DSV-based code. They found that for the dry bed test, both type of models were accurate, except for the earliest stages of propagation. For the wet case, the

10969837, 0, Downloaded from https://onlinelibrary.wiley.com/doi/10.1002/esp.5817 by Uni Federico Ii Di Napoli, Wiley Online Library on [20/03/2024]. See the Terms and Conditions (https://onlinelibrary.wiley.com/terms-and-conditions) on Wiley Online Library for rules of use; OA articles are governed by the applicable Creative Commons License

DSV results deviated from experimental results in the vicinity of the positive wave front during the initial stages. Kocaman et al. (2020) compared DSV and RANS based on simulations of a dam-break flow advancing in a smooth channel with a contracting reach. Their study found very good agreement between measured data and RANS. Some discrepancies were observed between experiments and DSV solution during the early stages of the reflected wave formation. Despite inaccurate prediction of the negative bore formation and overestimation of the peak water levels, the DSV model was still capable of predicting the free-surface profiles with an acceptable level of accuracy.

Based on systematic comparison of dam-break wave simulations over dry and wet bed, Yang et al. (2019) did not find a large sensitivity of the RANS solutions on the specific turbulence model used (e.g. standard $k-\epsilon$, RNG $k-\epsilon$ and $k-\omega$). Bigdeli et al. (2023) used RANS and LES approaches to simulate the laboratory experiments of Liu et al. (2020). Simsek and Islek (2023) implemented a 2D LES code to simulate dam-break waves with a downstream-to-upstream water depth ratio between 0 and 0.4.

One can conclude that DSV-based models can predict with a reasonable level of accuracy dam-break waves propagating over a bed containing no obstacles. However, 3D RANS and LES are needed to capture the finer flow features associated with large turbulence, air entrainment and the presence of hydraulic jumps.

The presence of a bluff obstacle increases significantly the flow three-dimensionality. For example, Kamra et al. (2018) conducted experiments and numerical simulations to study the impact of a dam-break wave against a vertical wall. They found that most of the flow three-dimensionality develops during the initial impact phase. Three-dimensional features were found to originate at the sidewalls and then propagate towards the inner regions of the domain. The main sources of three-dimensionality were as follows: the turbulence development and the region of high shear between the sidewall region and the inner region of the wave front during impact. Based on these considerations, the above-described criteria for choosing the appropriate modelling approach are not straightforwardly applicable.

Aureli et al. (2015) compared results obtained from 2D DSV model with those predicted by a 3D RANS model for the interaction of a dam-break wave with a single narrow-width obstacle. The study found that the error in the peak load for the 2D DSV model with respect to the 3D RANS model was of the order of 10%. Liu et al. (2020) analysed the propagation and impact of two- and three-dimensional dam-break waves using three different models: RANS, level I Green–Naghdi (GN) and DSV. They found that DSV models were quite inaccurate, while the RANS simulation reproduced fairly well the main physics. The accuracy of the GN simulation was similar to RANS, while the computational cost was less compared with RANS. Dai et al. (2020) performed a series of dam-break simulations based on the experiments of Xu et al. (2013) for a cascading dam failure using with both DSV and RANS with the $k-\epsilon$ turbulence model. They observed large errors when the traditional DSV equations were used to calculate the run-up height of the cascading dam failure. Recently, Ling et al. (2023) used both RANS and LES approaches to simulate three dam-break experiments involving obstacles. They compared the model predictions in terms of the water depth and impact load. Depending on the experimental condition, the former or the latter approach was found to give the best agreement with the experimental data. Overall, both RANS and LES predicted reasonably well the evolution of the dam-break wave following the impact as far as the global parameters were concerned.

The above literature survey highlights the need for additional detailed laboratory investigation of the interaction of impulse waves with obstacles that provide accurate and comprehensive data for validation of numerical models. It also shows the need for developing clear guidelines on the types of applications where DSV can provide accurate predictions and when the use of a 2D or 3D RANS model is required.

Moreover, the three-dimensional effects caused by the sidewalls (Kamra et al., 2018) need to be further analysed for problems involving the propagation of impulse waves in finite-width channels.

In the present paper, we try to address some of the above points. New laboratory investigations have been carried out reproducing a dam-break released in a rectangular channel with a nonerodible embankment in dry bed conditions. The goal is to investigate the wave impact with a rigid downstream end wall extending over the full channel width. The temporal variation of the pressure on the wall was measured to obtain the pressure distribution and the total force force acting on it.

The experimental results are compared with the numerical results obtained using three different numerical models of increasing complexity and computational cost. The choice of the most appropriate model is based on the three aspects cited above: three-dimensionality of the flow field, the capacity of the model to account for turbulence induced phenomena and for nonhydrostatic effects.

The simplest numerical model which we considered is based on the 1-D DSV approach that assumes an infinitely wide channel. We also performed hydrostatic and nonhydrostatic numerical simulations under two- and three- dimensional configurations. The hydrostatic numerical simulations are conducted using the Delft3D 4 Suite (structured) modelling software (Lesser et al., 2004). We used the STAR-CCM+ commercial package to conduct the RANS simulations with the VOF technique (Hirt & Nichols, 1981) to track the interface. For different initial water levels, numerical predictions are compared with the experimental data in terms of flow evolution and wave-induced pressure distribution and impact force on the vertical wall. We investigate the role of both turbulence and three-dimensional modelling in improving numerical predictions. This would be a proxy for planning more complex numerical studies, such as those considering a mobile bed and the consequent sediment transport processes (Di Cristo et al., 2020, 2021). The structure of the paper is as follows: the experimental setting is introduced in Section 2. The numerical models are described in Section 3. Section 4 presents the experimental investigation with a focus on the main hydrodynamic characteristics of the flow and successively the numerical results compared with experimental data. Finally, Section 5 presents the main conclusions.

2 | EXPERIMENTAL SETTING

A set of laboratory experiments has been carried out at the Hydraulics Lab of the University of Naples 'Federico II', in a rectangular Perspex channel, 2.92 m long, 0.4 m wide and 0.5 m high (Figure 1a). As indicated in Figure 1, the reference system has the x axis as the streamwise coordinate, the z axis is vertical, while the y axis is oriented along the spanwise direction. The channel is divided into two

10969837, 0, Downloaded from https://onlinelibrary.wiley.com/doi/10.1002/esp.5817 by Uni Federico Ii Di Napoli, Wiley Online Library on [20/03/2024]. See the Terms and Conditions (https://onlinelibrary.wiley.com/terms-and-conditions) on Wiley Online Library for rules of use; OA articles are governed by the applicable Creative Commons License

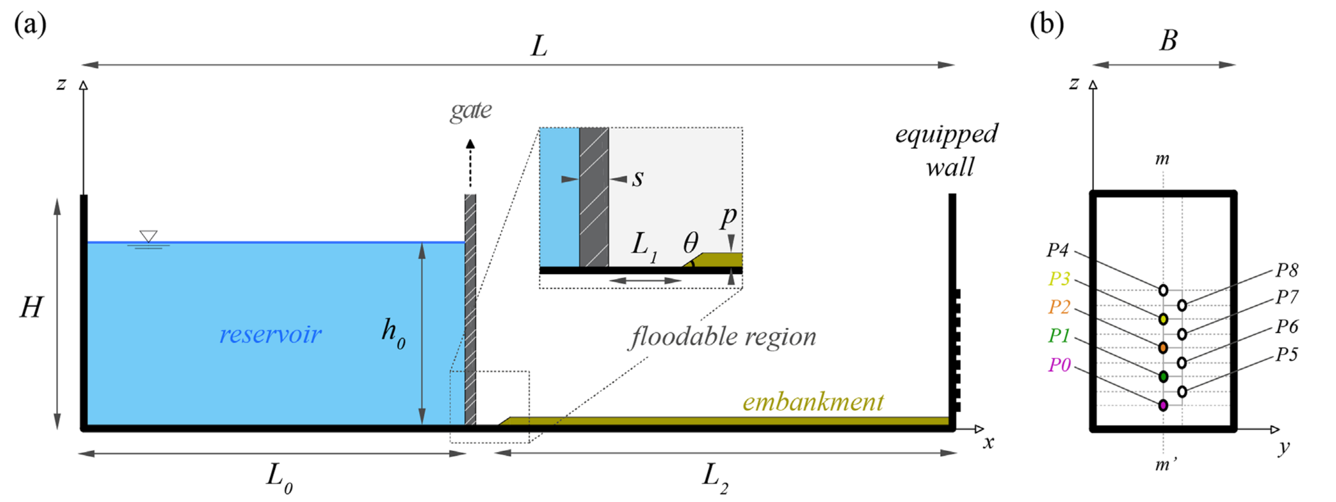

FIGURE 1 Sketch of the channel. (a) Lateral view (x-z plane). (b) Frontal view of the downstream wall (y-z plane), equipped with pressure transducers (P_i) distributed in nine nodes of a lattice composed by 9×4 lines spaced 0.02 m along both y and z directions. Transducer P_0 is placed at 0.01 m from the bottom along the wall centreline ($m-m'$)

regions by a movable lift gate: the reservoir on the left-hand side ($L_0 = 1.5$ m) and the floodable area on the right side, where a $L_2 = 1.36$ m fixed bed embankment is placed at $L_1 = 0.015$ m from the gate, which thicknes is $s = 0.04$ m. The bed embankment presents a short sloping boundary ($\theta = 45°$), followed by a $p = 0.025$ m high flat bottom. A full-width rigid wall is placed at the end of the channel. A hydrometric rod, with an accuracy of 0.5 mm, is used to fix the water level in the reservoir up to a defined value h_0. In three different initial conditions $h_0 = 0.16$ m, 0.2 m and 0.24 m have been considered. The dam-break wave develops as a pneumatic system suddenly lifts the gate. The lifting velocity of about 1.35 m/s allows the removal of the dam in a time, t_R, which is compared with the characteristic scale t_C (Lauber & Hager, 1998), defined as follows:

$$t_C = \sqrt{\frac{2h_0}{g}} \tag{1}$$

where g is the gravity. For all the runs $t_R < t_C$ (Table 1), such that the gate removal may be considered instantaneous (Lauber & Hager, 1998).

Each experiment was recorded by two high-speed 5 MegaPixel CCD cameras (Iron 250 Kaya Instruments) with a resolution of 2560 × 2048 and a maximum acquisition frame rate of 211 fps, which has CHIO 35 mm lenses. The cameras are horizontally aligned and placed perpendicularly to the channel in front of the gate and the downstream vertical end wall. The digital video recording software Norpix StreamPix 7 was used to control and synchronise the CCD cameras, which are connected to a frame grabber. The postprocessing of the two synchronous frames (performed by Matlab Toolbox Zh, 2000 and Matlab stereo camera calibrator Heikkila & Silvén, 1997) allowed to obtain, for each time step, a unique, referenced image devoid of focal distortion. Using image analysis, the instantaneous free-surface profiles were obtained with an accuracy of 1 mm.

The vertical end wall at the downstream end of the channel is equipped with nine Gefran TSA pressure transducers (P_i) (Figure 1b). As indicated in Figure 1, five transducers, P_0 to P_5, are vertically spaced with a 0.02 m interval along the channel centreline, with P_0 at

TABLE 1 Comparison between the characteristic time t_C and the removal time t_R for each initial water level h_0 considered in the present study.

Initial water level	Characteristic time	Removal time
h_0 (m)	t_C (s)	t_R (s)
0.16	0.18	0.11
0.20	0.20	0.13
0.24	0.22	0.17

0.01 m from the bottom. The transducers P_5 to P_8 are distributed along the vertical with the same 0.02 m spacing on the right of the centreline. Each transducer can sample pressures with and a maximum frequency of 2000 Hz and an accuracy of 0.5% on the full-scale output (0.1 bar). A data acquisition system (Labjack T7) reads and converts the resulting samples into digital numeric values that are analysed with Matlab (The MathWorks Inc., 2022). Each transducer was calibrated under hydrostatic conditions.

Cameras and transducers were synchronised with the computer timeline, and their acquisition frequency was set at 100 Hz.

The instantaneous impact force on the end wall induced by the dam-break wave was evaluated by integrating on the vertical axis the pressures measured by the transducers, assigning to each one the corresponding influence area of a B × 2 cm stripe. For cases $h_0 = 0.2$ m and $h_0 = 0.24$ m, the water level overcame the influence area of the pressure sensor $P4$ of about 2% and 4% of the total water depth on the wall, respectively.

The experimental repeatability has been verified by performing each test five times in the same experimental condition. The experimental results presented in Section 5 for the pressure and force acting on the end wall are obtained as the ensemble average of the values measured in the five tests performed for the same test condition. The averaged root mean square (RMS) of the pressure and force measurements are about 4% and 3.7%, respectively, for the three cases investigated in the present study. The the predicted accuracy of the peak force values were 5.03%, 5.10%, 7.34% for $h_0 = 0.16$, 0.20 and 0.24 m, respectively.

10969837, 0, Downloaded from https://onlinelibrary.wiley.com/doi/10.1002/esp.5817 by Uni Federico Ii Di Napoli, Wiley Online Library on [20/03/2024]. See the Terms and Conditions (https://onlinelibrary.wiley.com/terms-and-conditions) on Wiley Online Library for rules of use; OA articles are governed by the applicable Creative Commons License

10969837, 0, Downloaded from https://onlinelibrary.wiley.com/doi/10.1002/esp.5817 by Uni Federico Ii Di Napoli, Wiley Online Library on [20/03/2024]. See the Terms and Conditions (https://onlinelibrary.wiley.com/terms-and-conditions) on Wiley Online Library for rules of use; OA articles are governed by the applicable Creative Commons License

3 | NUMERICAL MODELLING

Experimental results are used to verify and compare the results of simulations carried out with different modelling approaches. The main features of the numerical models considered in the present study are summarised in Table 2. Both 2D and 3D simulations were performed using the hydrostatic multi-layer (HML) and the Navier–Stokes two-phase (NSTP) models.

3.1 | HML numerical model

The Delft3D 4 Suite (Lesser et al., 2004; Roelvink & Banning, 1995) is widely adopted to simulate hydrodynamics problems in which the horizontal length scales are significantly larger than the vertical ones (Christensen et al., 2020; La Forgia et al., 2022) (e.g. coastal areas, estuaries and rivers). Delft3D solves the RANS equations for an incompressible fluid assuming hydrostatic pressure distribution along the vertical direction. It therefore includes continuity, horizontal momentum and transport equations, along with a turbulence closure model (Dan et al.2011).

In the present study, we used the Delft3D 4 Suite for 1D, 2D (in the x-z plane) shallow water and 3D hydrostatic numerical simulations.

In the 2D and 3D simulations, the vertical velocities are computed from the continuity equation. Moreover, the model uses orthogonal curvilinear coordinates in the horizontal directions and a boundary-fitted σ coordinates system for the vertical z direction (σ-model) (Phillips, 1957). The Reynolds stress components are modelled as the product of grid-dependent eddy viscosity coefficients and the corresponding components of the mean rate-of-deformation tensor. The 1D simulations were performed without turbulence model. The numerical grid is composed of a single σ-layer along the z direction and 1171 square cells having a length of 2.5×10^{-3} m along the x direction. By using a free-slip condition for the lateral boundaries, the solved equations are fully equivalent to the 1D shallow flow equations of the DSV model.

The 2D hydrostatic, multi-layer numerical simulations (HML-2D) were performed on a mesh having the same cell size in the streamwise direction used in the 1D simulations A free-slip condition was imposed at the lateral boundaries. A multi-layer discretisation was used along the z direction by defining 64, 80 and 96 σ-type cells in the simulations performed with $h_0 = 0.16$, 0.2 and 0.24, respectively. Eddy viscosity coefficients were obtained using the $k-\epsilon$ turbulence model (Burchard & Baumert, 1995).

A no slip condition was imposed at the lateral boundaries in the HML-3D simulations. The computational domain contained 1171×163 squared cells having a size of 2.5×10^{-3} m in the streamwise and vertical directions. The same number of σ-type cells adopted in the corresponding 2D simulations was used. The grid resolution has been chosen to provide mesh-independent results through a sensitivity analysis comparing the time evolution of the impact force from simulations conducted with different levels of mesh refinements. The sensitivity of the temporal behaviour of the simulated impact force to the level of mesh refinement can be inferred from in Figure 2a,b for HML-2D and HML-3D simulations, respectively. The computational time step was kept constant (6×10^{-4} s) to guarantee the local Courant number less than 1.

In all simulations, a Chezy coefficient of 68.9 $m^{1/2}s^{-1}$ was used for the bottom roughness.

3.2 | NSTP numerical model

The 2D and 3D NSTP simulations were performed using the STAR-CCM+ commercial package. A pressure-Poisson equation is solved for the nonhydrostatic pressure (Wilcox, 1998), and the SIMPLE algorithm (Patankar, 2018) is used to integrate the RANS equations. The two-layer $k-\varepsilon$ model is used to calculate the eddy viscosity (Wilcox, 1998). The free-surface position is obtained using the VOF method (Hirt & Nichols, 1981), which can successfully deal with overturning flows, allowing air entrainment, bubble formation and complex free-surface distortions. A layer of air is present in the upper part of the entire computational domain. In VOF, a pure-advection equation is solved for the volume fraction of water in a cell, V_f. In cells containing only water $V_f = 1$, while in cells containing only air $V_f = 0$.

The advective terms are discretised using a second-order accurate upwind scheme, while the diffusive and pressure gradient terms are discretised using the second-order, central-differences scheme. The implicit temporal discretisation is also second-order accurate. The first-order upwind scheme is used to discretise the convective terms in the transport equations for k and ε (Munoz & Constantinescu, 2020). Due to the nonlinear nature of the problem, a two-loop iterative solution is employed: an outer loop controlling the solution update and an inner loop governing the iterative solution of the linear system, which is accomplished using algebraic multigrid

TABLE 2 Main features of the numerical models considered in the present study.

	De Saint-Venant model	Hydrostatic multi-layer model	Navier–Stokes two-phase model
Pressure distribution	Hydrostatic	Hydrostatic	non-hydrostatic
Phase	water	water	air and water
Dimension	1D	2D and 3D	2D and 3D
Turbulence modelling	–	$k-\varepsilon$	$k-\varepsilon$
Notation	DSV	HML-2D and HML-3D	NSTP-2D and NSTP-3D
Processor	INTEL i7-7700 3.60 GHz	INTEL i7-7700 3.60 GHz	Argon HPC
RAM	48 GB	48 GB	28 nodes of 4 GB per core
Simulation time	0.1 h	1 h (2D) - 16 h (3D)	2 h (2D) - 120 h (3D)

Note: Hardware configuration and average computational time are reported for each simulation.
Abbreviations: DSV, De Saint-Venant equation; HML, hydrostatic multi-layer; NSTP, Navier–Stokes two-phase.

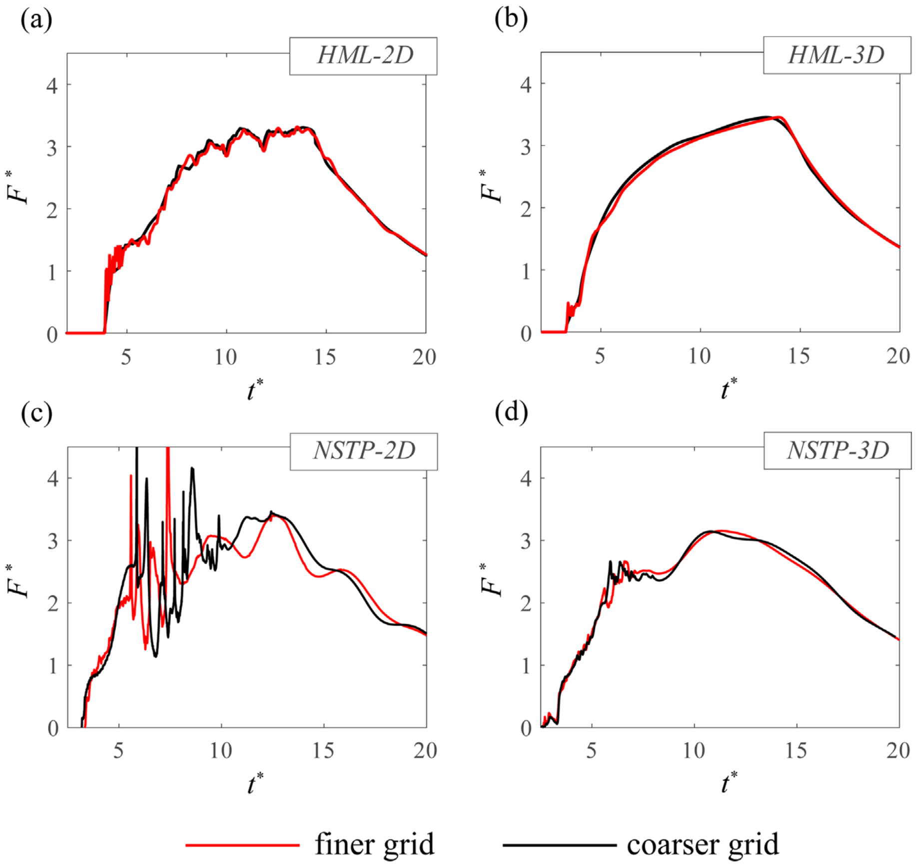

FIGURE 2 Time impact force F^* per unit width is used for the mesh refinement study for (a-, b) HML models and (c, d) NSTP models. The fine mean grid is 3 mm, and the coarse mean is 5 mm. HML, hydrostatic multi-layer; NSTP, Navier–Stokes two-phase.

(AMG). The viscous solver in STAR-CCM+ is parallelised using MPI and has shown good scalability on large PC clusters (Munoz & Constantinescu, 2020).

In the NSTP-3D simulations, the mean mesh size is 5×10^{-3} m in all three dimensions, which corresponds to about 950 wall units when normalised with the maximum bed friction velocity (u_τ). The mesh was refined close to the bottom and near the lateral and downstream walls, with the refinement generated by means of eight prism layers. At these solid surface, the cell size in the wall normal direction was 1.5×10^{-4} m corresponding to about one wall unit. The mesh contained a total of about 2.69×10^{6} cells. At the top boundary, where only air is present, a pressure outlet boundary condition was imposed, which is standard treatment for this type of two-phase flows. The velocity was set equal to zero on all the solid surfaces, and the surfaces were assumed to be smooth. A constant time step was used corresponding to a maximum CFL number of 0.2. The mesh in the NSTP-2D simulations was the same as that used in a $y=$ constant plane in the corresponding NSTP-3D simulations and contained close to 0.9×10^{5} cells. For the NSTP simulations, the grid resolution has been chosen based on a sensitivity analysis. As shown in Figure 2c,d for the NSTP-2D and NSTP-3D simulations, respectively, the computed time history of the impact force does not vary significantly with the level or mesh refinement once the grid is finer than the one used in the coarse grid simulations.

4 | RESULTS

For each simulation conducted with the different numerical models (Table 2), we computed the water depth profiles and the temporal evolution of the pressure induced by the dam-break wave on the vertical end wall. For the 3D simulations, the reported depth profiles and pressure evolution refer to the channel centreline. Moreover, we estimated the force acting at the centreline of the wall by integrating the instantaneous pressure distribution derived from numerical results. This allowed us to compare forces measured from Experiments (LabExp in Section 2) with those predicted by the numerical simulations.

4.1 | Flow dynamics

The dynamics of the dam-break wave observed in the laboratory experiments is discussed considering the following dimensionless variables:

$$t^*=\frac{t}{t_c},z^*=\frac{z}{h_0},x^*=\frac{x}{h_0},P^*=\frac{P}{P_c},F^*=\frac{F}{F_c}, \tag{2}$$

where t_c is defined by Equation (1), $P_c=\gamma h_0, \gamma=9810\ \mathrm{Nm^{-3}}$ is the specific weight of water and $F_c=0.5\gamma h_f^2, h_f$ is the water level at the vertical end wall at the end of each experiment, that is, when water is at rest.

In what follows, we report the flow features observed for the $h_0=0.2$ m experiment, which is also representative of the wave dynamics for the other cases. Figure 3 shows the measured free-surface profile along the channel at different time instants. The main flow process develops within a temporal window that ranges from $t^*=0$, when the lock gate is removed, to $t^*=20$, when the dam-break wave is almost completely reflected.

Figure 4 depicts the temporal evolution of the water level, pressure and force measured at the end wall. For a better readability of

10969837, 0, Downloaded from https://onlinelibrary.wiley.com/doi/10.1002/esp.5817 by Uni Federico Ii Di Napoli, Wiley Online Library on [20/03/2024]. See the Terms and Conditions (https://onlinelibrary.wiley.com/terms-and-conditions) on Wiley Online Library for rules of use; OA articles are governed by the applicable Creative Commons License

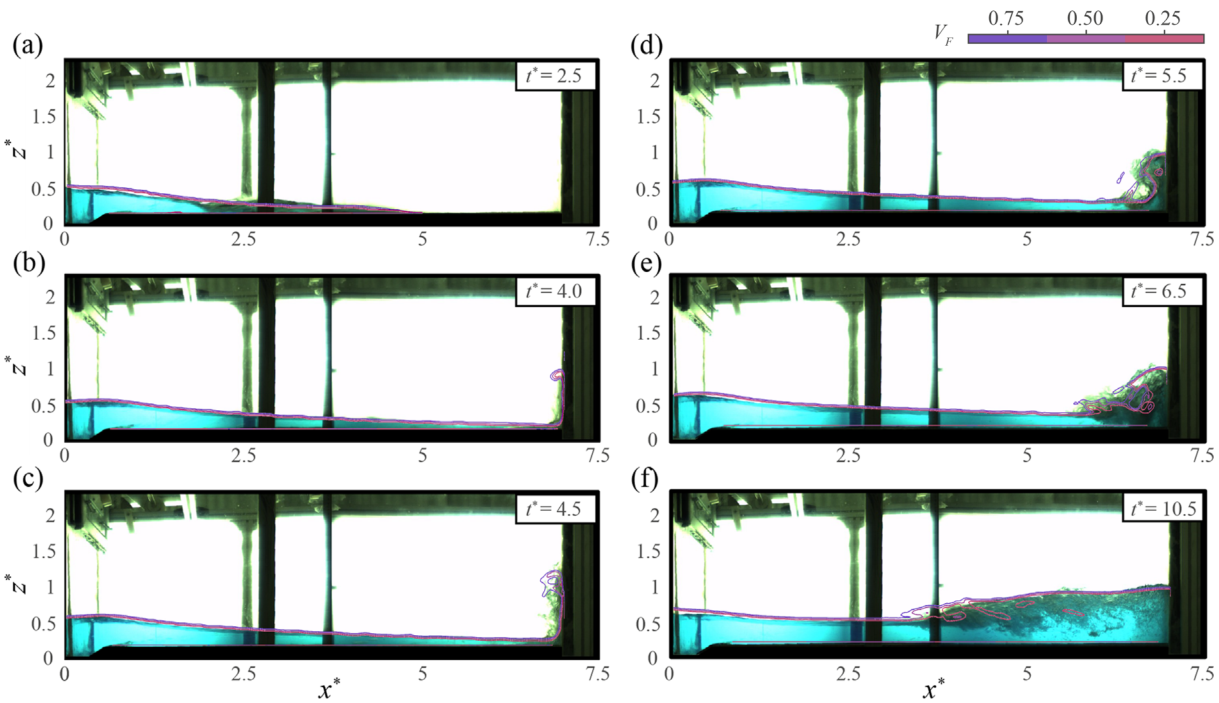

FIGURE 3 Flow evolution for the $h_0 = 0.2$ m case. Methylene blue is dissolved into the water to improve image readability. Contour lines represent volume fractions $V_f = 0.25$, 0.5 and 0.75, predicted by the corresponding NSTP-3D simulation. NSTP, Navier–Stokes two-phase.

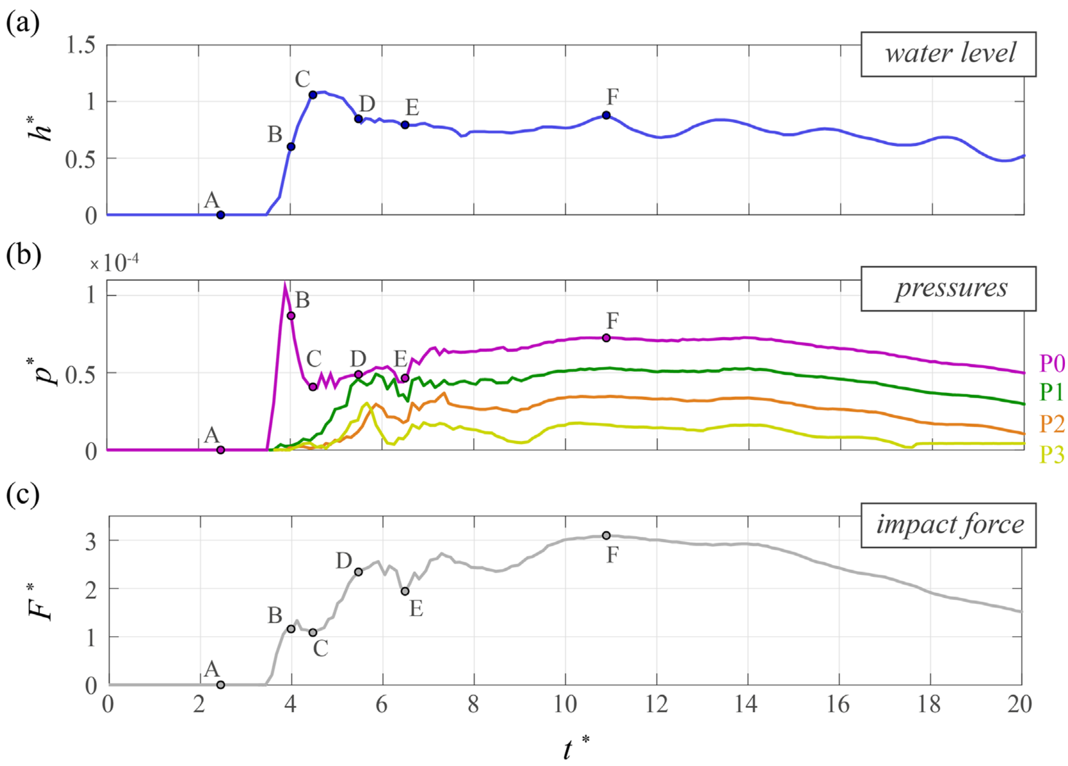

FIGURE 4 Time histories of the reference quantities measured in the $h_0 = 0.2$ m experiment: (a) water level h^* on the vertical wall obtained from image analysis; (b) pressures p^* sampled from transducers P_0-P_3; (c) impact force F^* per unit width acting on the vertical wall along $m-m'$. Data are estimated by averaging measurements derived from five repetitions of the experiment for each case. Quantities associated to the snapshots shown in Figure 3 are marked by circles and identified by the corresponding capital letters (i.e. A-F)

the plot, the measurement of the highest transducer P_4 is not reported in Figure 4b. Its contribution is about 4% of the total force. After the gate removal, the wave starts propagating downstream and it reaches the end wall at $t^* = 3.6$ (Figure 4a). The wave collision against the wall produces a vertical jet that is observed to run up the end wall (Figure 3b). The transducer closest to the bottom (i.e., P_0) measures a localised pressure increment for a relatively short period of time, of about 0.5 t^* (red curve in Figure 4b), during which the pressure signal resembles a Dirac delta function (Bredmose et al., 2010; Hattori et al., 1994; Peregrine, 2003), peaking at approximately

10969837, 0, Downloaded from https://onlinelibrary.wiley.com/doi/10.1002/esp.5817 by Uni Federico Ii Di Napoli, Wiley Online Library on [20/03/2024]. See the Terms and Conditions (https://onlinelibrary.wiley.com/terms-and-conditions) on Wiley Online Library for rules of use; OA articles are governed by the applicable Creative Commons License

$t^* = 3.9$ (Figure 4b). When the vertical water jet changes direction, the pressure levels recorded by the higher transducers (Figure 4a) are considerably lower than P_0 (Figure 4b). Their small contribution to the total force is due to dynamic pressure. Indeed, velocity vectors are expected to be horizontally oriented in the proximity of the bottom (i.e. near P_0) and moving away from it (i.e. inside body of the vertical jet). For this reason, the first stage of the collision is mostly impulsive and governed by inertial forces: the load acting on the end wall is mainly produced by the dynamic pressures acting near the bottom, as indicated by the comparison of the pressure and force variations in Figure 4b,c for $t^* < 4$.

Later on, the water level close to the end wall continues to increase, reaching its maximum elevation at $t^* = 4.5$ (Figures 3c and 4a). During this, the pressure at P_0 reduces to about 50% of its maximum value (Figure 4b), while those recorded by the other transducers show only a slight increase. As a result, the the total load on the end wall shows a local minimum at $t^* = 4.5$ (point C in Figure 4c) which, surprisingly, corresponds to the time when the water level at the end wall is the highest (point C in Figure 4a). This is probably due to the fact that only a part of the water column is actually in contact with the end wall. For $4.5 < t^* < 5.5$, the flow depth decays (Figure 4a) because the jet head gradually detaches from the wall as it overturn backward (Figure 3d). This seems to be inconsistent with the fact that the transducers record their largest pressures during the same time interval (Figure 4b). However, during this time, additional water released from the reservoir reaches the wall, increasing the thickness of the water layer located below the vertical jet (compare Figure 3c,d at $x^* \simeq 6.5$). As a result, the region close to the wall containing horizontal velocities becomes thicker. This shows that, during this stage, the dynamic pressure components play again a crucial role in determining the load transferred to the end wall (see Figure 4c between points C and D).

As time passes, the jet evolves in a counterclockwise vortex which interacts with the incoming body of the dam-break wave, causing a large amount of air entertainment (Figure 3e). In response to this mixing process, the measured pressures and the estimated force exhibit oscillations and irregular pulsations (see Figure 4a,b for $t^* > 5.5$). The dam-break wave is partially reflected, and the newly formed bore propagates backward (Figure 3e,f). During this phase, multiple, rank-ordered Favre waves (Favre, 1935) propagating downstream are released from the surge tail. For $t^* > 10$, the water level at the end wall gradually decreases, while the Favre waves induce local oscillations of the water level (Figure 3e) and pressures measured by the transducers (Figure 4b). At $t^* = 10.5$, as the first Favre wave is reflected by the end wall (Figure 3f), the force acting on the wall reaches its maximum value (point F in Figure 4c). Although successive oscillations develop near the end wall (i.e., for $t^* > 10.5$), the impact force gradually attenuates in response to decreasing water levels (Figure 4a,c).

4.2 | HML numerical simulations

The HML results are compared with experimental data in terms of water front celerity, pressure and forces acting on the end wall.

Figure 5 compares the Hovmoller diagrams of the water depth in the $x^* - t^*$ plane derived from laboratory experiments and the HML-2D and 3D-HML simulations, in which the solid lines represent the dam-break wave front based on the DSV-1D simulations. Figure 5 indicates that the wave front celerity is well captured by the DSV-1D, HML-2D and HML-3D simulations during the propagation of the incident wave ($t^* = 0 - 5$), as also confirmed by the accurate prediction of the impact time (Figure 5b,c). Since the HML models assume negligible vertical accelerations, they cannot reproduce several peculiar flow processes of the wave–structure interaction. In particular, the HML simulations do not capture the formation of vortical structures in the vertical plane nor air entrainment from the free surface. This is also confirmed by the comparison of the temporal histories of the pressure acting on the end wall predicted by the simulations with the experimental data reported in Figure 6. The inability of the HML simulations to capture the details of the flow physics in regions where the shallow flow assumptions are not satisfied is the main reason why the instantaneous front position of the reflected wave shows a regular and continuous trend for $t^* > 5$ that departs from the experimental measurements (compare Figure 6b,c with 6a). The HML-3D model is not able to reproduce the oscillatory behaviour of the pressure during the initial impact phase (Figure 6a,b for $3.9 < t^* < 12$), with the simulation data showing a monotonic increase until a maximum value is reached. The oscillations predicted in the HML-2D simulations (Figure 6c for $3.9 < t^* < 12$) have higher frequencies than those in the HML-3D simulations and may be due to the suppression of vortex stretching in the spanwise direction. This produces nonphysical, high-frequency pressure oscillations not observed in the 3D simulations where vortex stretching is possible. Still, these spurious oscillations in the 2D simulations do not change the overall behaviour of the pressure time series in the two types of simulations. The peak values of the pressure are very close in the 2D and 3D HML simulations. The temporal decrease of the pressure after the peak value is reached is well-reproduced by both 2D and 3D simulations. Due to the hydrostatic pressure distribution assumption, both HML models do not capture the first pressure peak measured at $t^* = 3.9$ by the P_0 transducer (Figure 6a).

Figure 7 shows the time history of the dimensionless force predicted by the DSV-1D model and the one obtained from experiments for the three cases. The error bars, representing the RMS evaluated based on the five repetitions of the same test, are also reported. It can be noted that the DSV-1D simulation reproduces with a sufficient accuracy the impact time and the magnitude of the peak force, with a difference of about 10% for the maximum sampled value.

Figure 8 compares the temporal evolution of the dimensionless impact forces predicted by the HML-2D and HML-3D simulations and those obtained form the experiments. As also the case for the pressure, the HML-3D simulations predict an approximately monotonic increase of the force until a maximum value is reached, without reproducing the oscillatory behaviour observed in the experiments (Figure 8a–c for $5 < t^* < 12$). The force evolution predicted by the HML-2D simulations for the $h_0 = 0.16$ m and $h_0 = 0.24$ m cases is in better agreement with the experimental data. However, these oscillations are numerical artefacts rather than a result of correctly capturing the flow physics. This is confirmed by comparing 2D simulation results and experimental measurements in the $h_0 = 0.20$ m case at $t^* < 10$, where a greater discrepancy with the experimental data is observed. Both 2D and 3D HML simulations overestimate by about 10% the

10969837, 0, Downloaded from https://onlinelibrary.wiley.com/doi/10.1002/esp.5817 by Uni Federico Ii Di Napoli, Wiley Online Library on [20/03/2024]. See the Terms and Conditions (https://onlinelibrary.wiley.com/terms-and-conditions) on Wiley Online Library for rules of use; OA articles are governed by the applicable Creative Commons License

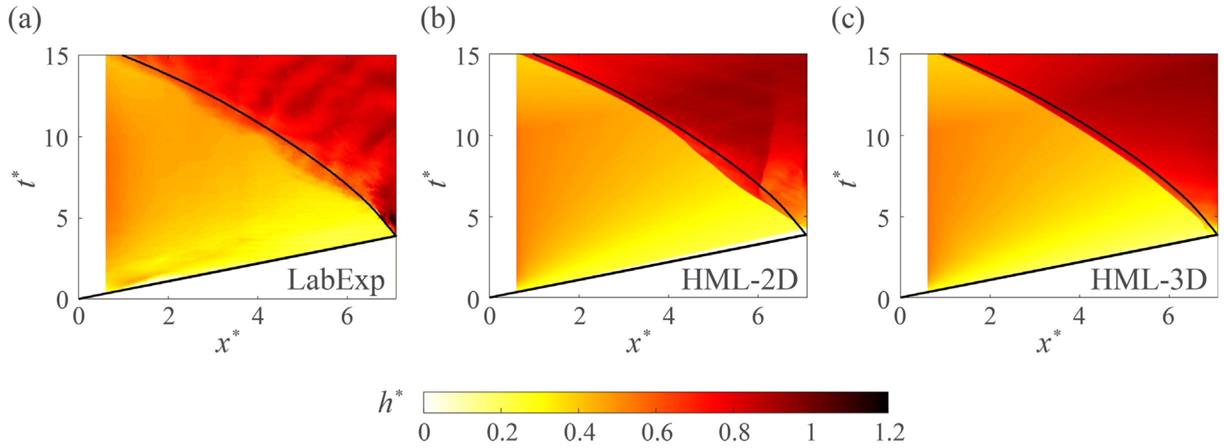

FIGURE 5 Hovmoller diagrams in the $x^* - t^*$ plane of the water depth h^* for the $h_0 = 0.2$ m case. from (a) laboratory experiments (LabExp) (b) two-dimensional (HML-2D) simulations and (c) three-dimensional (HML-3D) simulations. Solid lines refer to the dam-break wave front predicted by one-dimensional DSV simulations. DSV, De Saint-Venant equation; HML, hydrostatic multi-layer.

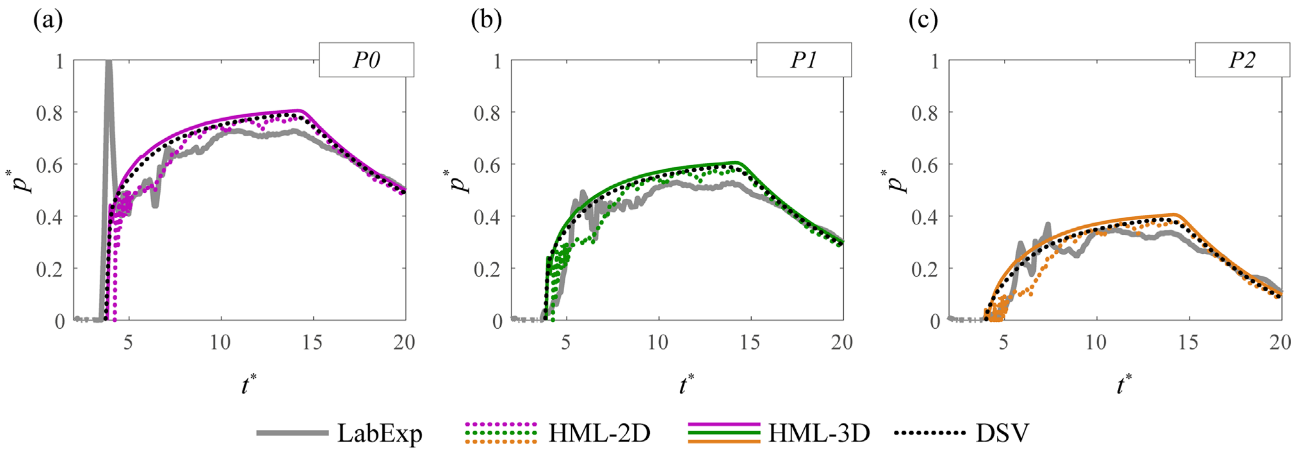

FIGURE 6 Time histories of the nondimensional pressure in the $h_0 = 0.2$ m case at points (a) P_0, (b) P_1 and (c) P_2, derived from laboratory experiments (grey thicker lines), HML-2D (dotted lines) and HML-3D (solid lines) simulations. The colours refer to pressure gauges locations as depicted in Figure 1b. HML, hydrostatic multi-layer.

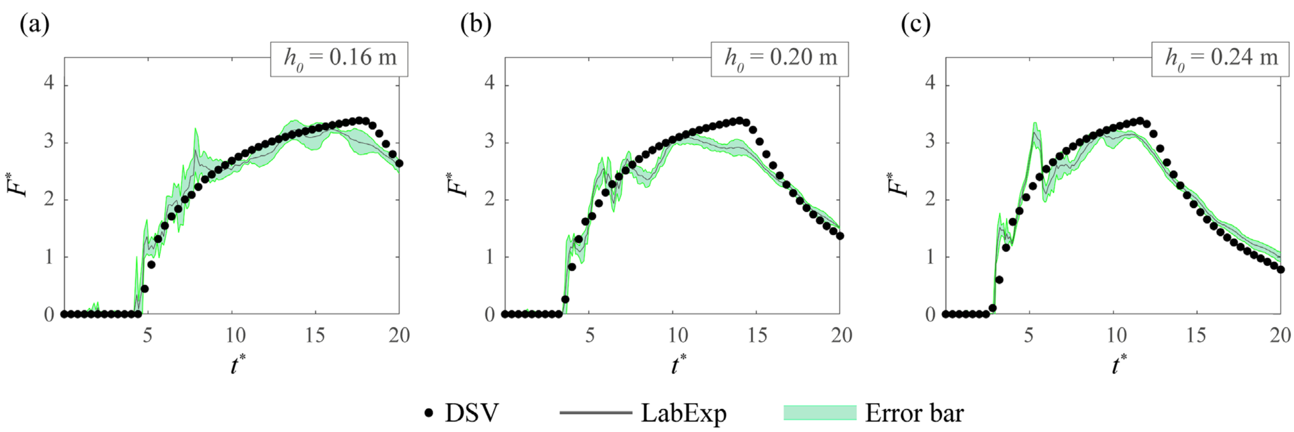

FIGURE 7 Time histories of the nondimensional impact forces for the cases with (a) $h_0 = 0.16$ m, (b) $h_0 = 0.2$ m and (c) $h_0 = 0.24$ m. Forces are estimated from DSV simulations (black dots) and laboratory experiments (grey line). The green-shaded areas represent the 68% confidence interval of the experimentally average values. DSV, De Saint-Venant equation.

10969837, 0, Downloaded from https://onlinelibrary.wiley.com/doi/10.1002/esp.5817 by Uni Federico Ii Di Napoli, Wiley Online Library on [20/03/2024]. See the Terms and Conditions (https://onlinelibrary.wiley.com/terms-and-conditions) on Wiley Online Library for rules of use; OA articles are governed by the applicable Creative Commons License

maximum force acting on the end wall. Meanwhile, these simulations accurately capture the further decrease of the pressure after the peak was reached (Figure 8a–c).

4.3 | NSTP numerical simulations

A similar analysis of the time histories of the pressure and total impact force on the end wall is carried in this section for the 2D and 3D NSTP simulations.

Figure 9 shows the Hovmoller diagrams of the water depth in the $x^* - t^*$ plane for the laboratory experiments, the NSTP-2D and the NSTP-3D simulations in which the solid line represents the dam-break wave front based on the DSV-1D simulations. In terms of free-surface evolution, the NSTP-3D simulations show a very good agreement with experimental data during both the incident wave phase when the front celerity is accurately captured by the simulations and during the impact phase. At later times, we observe relatively small discrepancies in terms of the free-surface oscillations induced by the Favre waves (compare Figure 9a,c at $t^* > 8$ and $4 < x^* < 7$). We tested in more detail the predictive accuracy of the NSTP-3D simulation by superimposing the contour lines associated with different values of the volume fraction V_f to the corresponding experimental images (Figure 3). The VOF technique implemented for tracking the free surface allowed reproducing all the main flow features observed experimentally during the wave–structure interaction: flow overturning, air entrainment and formation of air bubbles. Indeed, for the $h_0 = 0.2$m, the free-surface evolution during the incident phase (Figure 3a,b) and the wave–structure interaction (Figure 3c,d) is very well predicted by the numerical simulation. During the reflection stage, instead, the predicted free-surface profile shows a more monotonic behaviour compared with the experimental one. The last phase shows more pronounced Favre waves developing above the backward-propagating bore in the 3D simulation (Figure 3e,f).

The NSTP-2D simulation accurately reproduces both the incident wave front celerity and the impact time against the wall (Figure 9b). Overall, the spatio-temporal evolution of the water depth derived from the NSTP-2D simulation (Figure 9b) is also in good agreement with experimental data (Figure 9a) during the reflection phase (i.e. for $t^* > 5$).

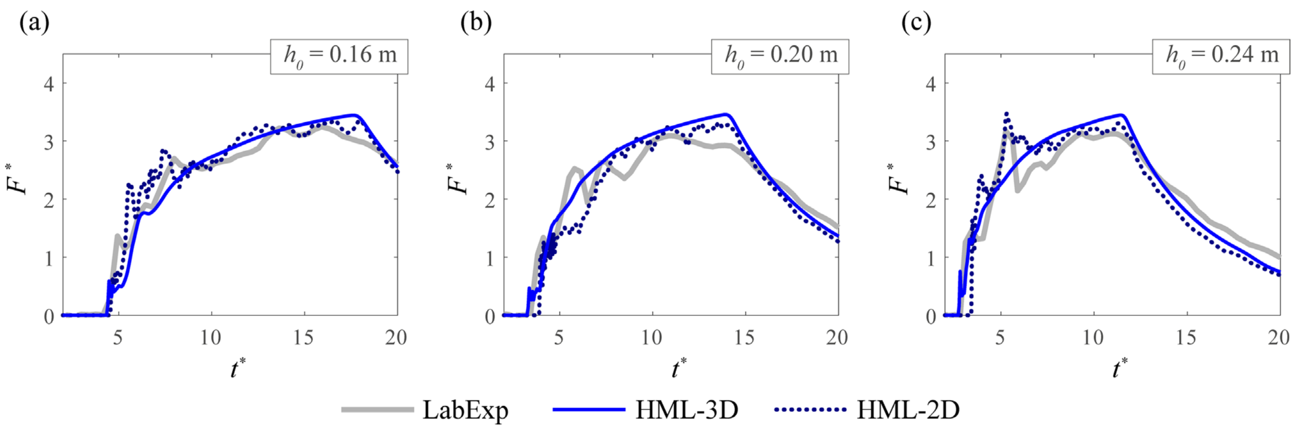

FIGURE 8 Time histories of the nondimensional impact forces for the cases with (a) $h_0 = 0.16$ m, (b) $h_0 = 0.2$ m and (c) $h_0 = 0.24$ m, derived from laboratory experiments (grey thicker lines), HML-2D (dotted lines) and HML-3D (solid lines) numerical simulations. HML, hydrostatic multi-layer

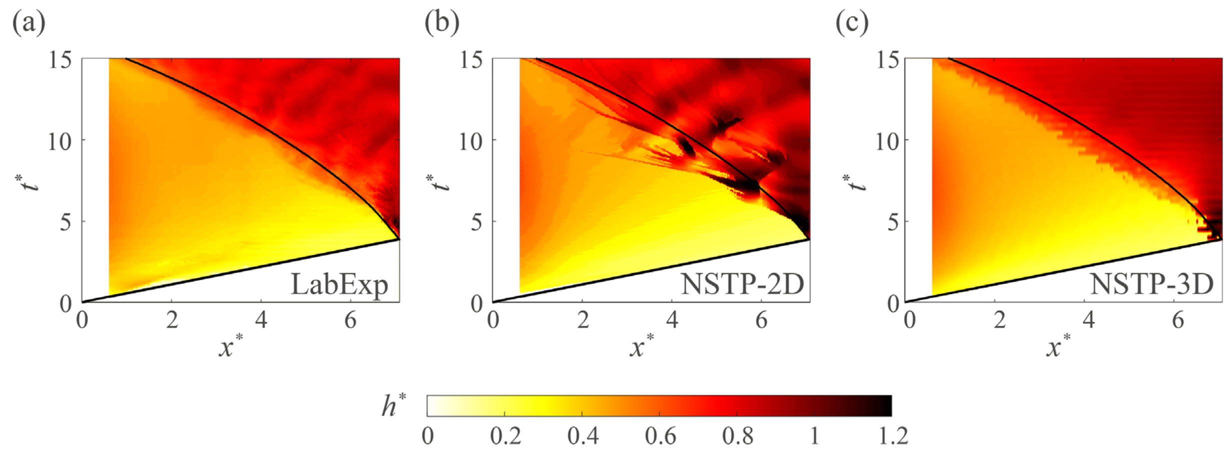

FIGURE 9 Hovmoller diagrams in the $x^* - t^*$ plane of the water depth h^* for the $h_0 = 0.2$ m case from (a) laboratory experiments (LabExp) (b) two-dimensional (NSTP-2D) simulations and (c) three-dimensional (NSTP-3D) simulations. Solid lines refer to the dam-break wave front predicted by the one-dimensional DSV simulations. DSV, De Saint-Venant equation; NSTP, Navier–Stokes two-phase.

10969837, 0, Downloaded from https://onlinelibrary.wiley.com/doi/10.1002/esp.5817 by Uni Federico Ii Di Napoli, Wiley Online Library on [20/03/2024]. See the Terms and Conditions (https://onlinelibrary.wiley.com/terms-and-conditions) on Wiley Online Library for rules of use; OA articles are governed by the applicable Creative Commons License

It is worth noting that during the impact phase, the jet falling backward into the incoming water generates three-dimensional flow features (Figure 3d–f). However, the NSTP-2D model does not allow vortex stretching and energy dissipation to take place along the spanwise direction. The resulting energy surplus generates a stronger 2D vortex that induces large oscillations of the free surface in the region $x^* = 4 - 5$ (Figure 9b). This is the main reason why the NSTP-2D predictions slightly overestimate the celerity of the backward-propagating bore for all of the three initial conditions considered in the present study. Moreover, the 2D simulation overestimates the water depths after the wave reflects at the end wall (e.g. see regions with $h^* > 1$ in Figure 9b).

In NSTP-3D simulations, vortex stretching takes place, which results in more realistic predictions of the pressure and impact force compared to those given by the NSTP-2D simulations. This is evident from Figures 10 and 11, which compare the measured and simulated pressure on the end wall and the impact force, respectively. The time histories of the pressure predicted by the NSTP-3D simulations are in excellent agreement with the measured ones, while for the NSTP-2D simulations predict more pronounced minima and maxima with non-realistic high frequency (Figure 10a–c). As noticed for the free-surface oscillations predicted by the NSTP-2D simulations, we argue that the pressure distribution is considerably affected in the 2D simulations by the lateral constraints that do not allow energy dissipation and vortex stretching to take place along the spanwise direction. Figure 12 compares the pressure values at three time instants during the early stages of the interaction of the wave with the end wall. As the wave reaches the end wall (Figure 12a), the total pressure reaches a relative maximum near the channel bottom (Figure 10b,c) that suddenly decreases in magnitude at later times (Figure 12c,f,i). At these times, the hydrostatic components are almost negligible with respect to the total pressure (Figure 12c,f,i). As the wave runs-up on the end wall, it forms a vertical jet that reaches a maximum elevation of about $z^* = 1$ (Figure 12d–g). During this phase, the pressure distributions show that only a portion of the water column generates a load on the vertical wall (Figure 12e–h), which may look surprising. During the run-up, the head of vertical jet does not completely touch the wall, being mainly characterised by vertical velocity components. As a result, although the jet head remains in contact with the end wall, it does not produce any significant load on the wall. The impact force predicted by the NSTP-3D simulations is almost identical to that obtained from measurements (Figure 11a–c) This is not true for the NSTP-2D simulations where several spikes associated with nonphysical oscillations are observed. The absolute maximum values of the impact force are

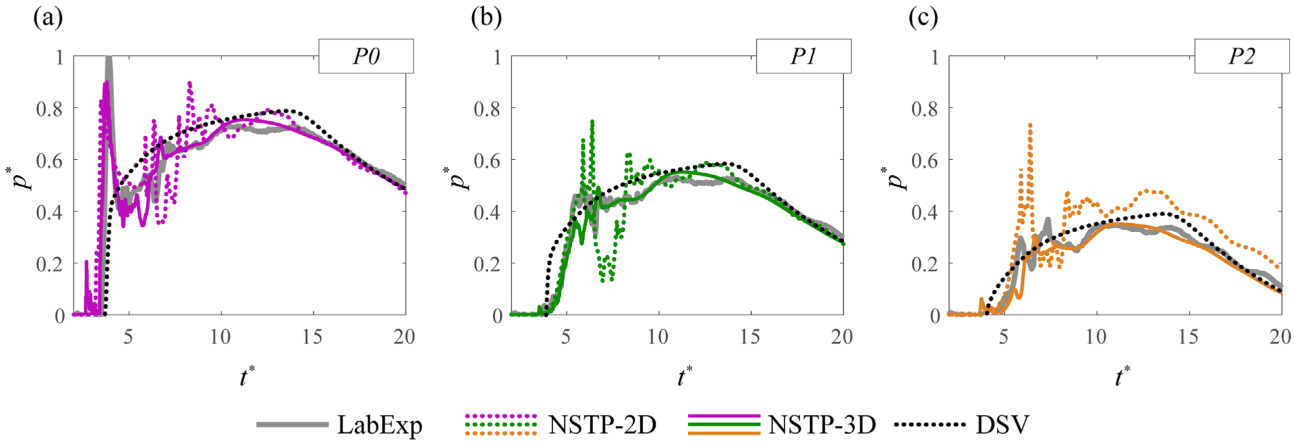

FIGURE 10 Time histories of the nondimensional pressure in the $h_0 = 0.2$ m case at points (a) P_0, (b) P_1 and (c) P_2, derived from laboratory experiments (grey thicker lines) and predicted by NSTP-2D (dotted lines) and NSTP-3D (solid lines) numerical simulations. Colours refer to pressure gauges locations as depicted in Figure 1b. NSTP, Navier–Stokes two-phase.

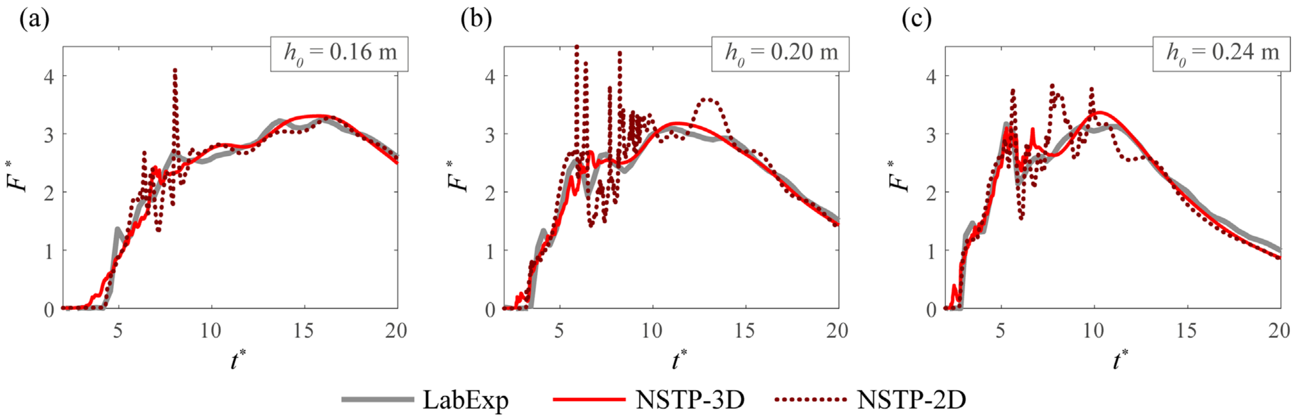

FIGURE 11 Time histories of the nondimensional impact forces for case (a) $h_0 = 0.16$ m, (b) $h_0 = 0.2$ m and (c) $h_0 = 0.24$ m. Forces are estimated from laboratory experiments (grey thicker lines), and from NSTP-2D (dotted lines) and NSTP-3D (solid lines) numerical simulations. NSTP, Navier–Stokes two-phase.

10969837, 0, Downloaded from https://onlinelibrary.wiley.com/doi/10.1002/esp.5817 by Uni Federico Ii Di Napoli, Wiley Online Library on [20/03/2024]. See the Terms and Conditions (https://onlinelibrary.wiley.com/terms-and-conditions) on Wiley Online Library for rules of use; OA articles are governed by the applicable Creative Commons License

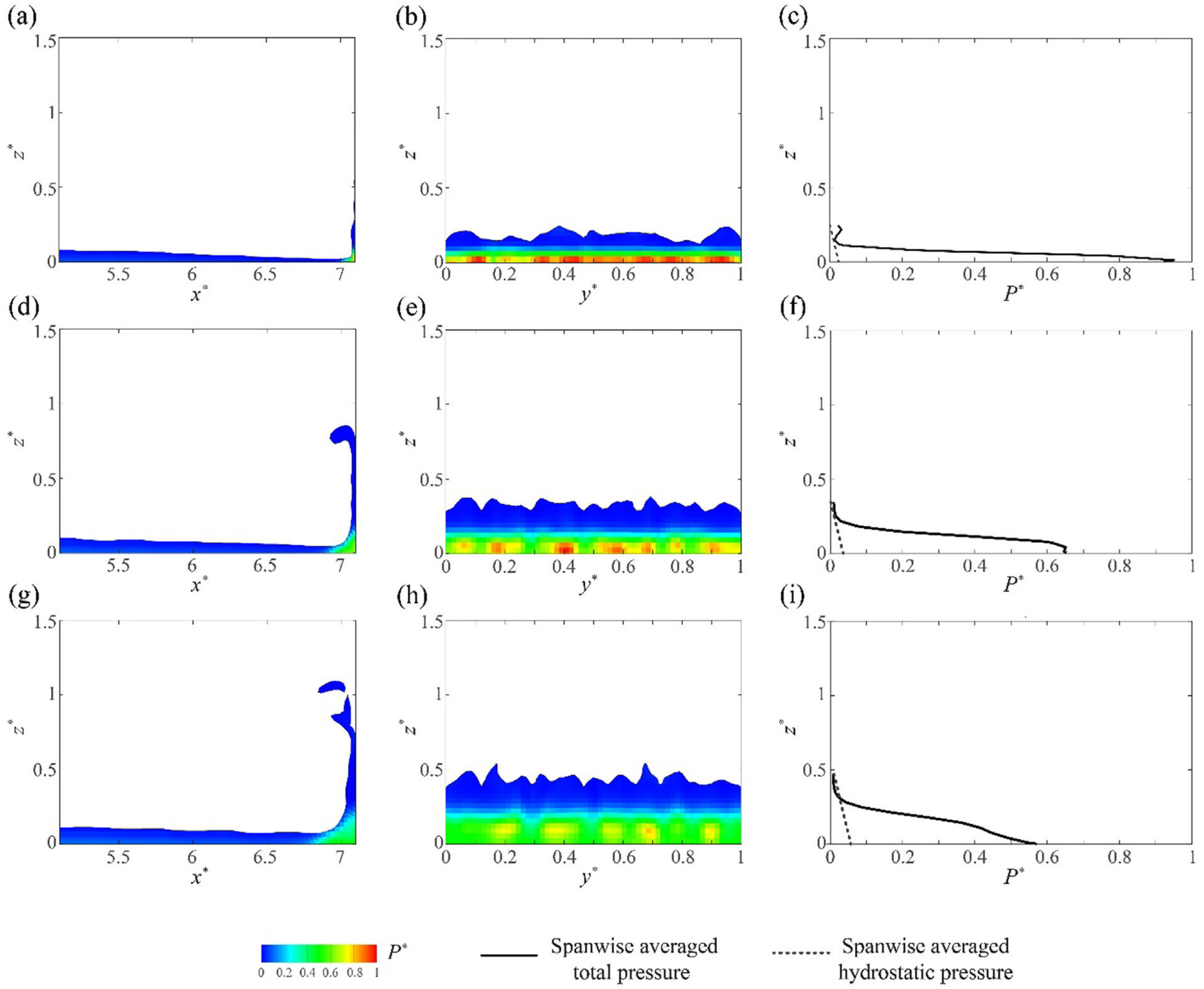

FIGURE 12 Early stages interaction between the dam-break wave and the vertical end wall for the $h_0 = 0.2$ m case, at three successive time steps: (a–c) $t^* = 3.5$, (d–f) $t^* = 4$ and (g–i) $t^* = 4.5$. Total pressure distribution in the x^*-z^* plane (a,d,g) and on the vertical end wall (b,e,h); Spanwise averaged total pressure (solid lines) and hydrostatic pressure (dashed lines) at the vertical end wall (c,f,i)

within 3% of the measured values in all three 3D simulations. By contrast, the errors are of the order of 20% in the 2D simulations because of the presence of the spikes. Therefore, to obtain good predictions of the time-varying local pressures and total force acting on the downstream wall, it is thus crucial to account for three-dimensional effects.

4.4 | Predictive capabilities of numerical models based on 3D simulations

Considering the overall better performance of the 3D simulations, we herein compare the accuracy of the HML-3D and NSTP-3D models. For a more thorough comparison, Figure 13 shows the three-dimensional free surface predicted by the two models at several time instants, while Figure 14 compares the temporal evolution of the impact force in these simulations together with results based on experimental measurements and the 1D DSV model prediction.

The NSTP-3D simulation provides the best physical description of the whole dam-break process (Figure 13d–f). It is able to capture vortex-stretching phenomena, air entrainment during and after the impact phase observed in the experiments (Figure 3). The plots also show the strong free-surface deformations in transversal direction, indicating a three-dimensional behaviour.

By contrast, the HML-3D simulation does not capture the counter-rotating vortex that forms in the experiment around $t^* = 10.5$ and predicts the formation of a a steep and flat backward-propagating bore (Figure 13a–c).

The pressure distribution predicted by the NSTP-3D simulation on the end wall is primarily nonhydrostatic during the impact phase (Figure 12c,f,i). For this reason, the HML-3D simulations are not able to reproduce well the pressure evolution, during the early stages of the wave–structure interaction (see Figure 6a–c). Only for $t^* > 15$, as the pressure distribution in the flow becomes close to hydrostatic, the pressure predicted by the HML-3D simulations shows good agreement with the experimental data. For all cases, the NSTP-3D predictions of the impact force are almost superposed on the curve derived from the experiments By contrast, the HML-3D simulation (Figure 14) shows relatively large errors during the impact phase. For $t^* > 10$, the backward-propagating bore develops and the vertical accelerations near the end wall gradually disappear. Once this happens, the hydrostatic pressure distribution becomes more realistic and the HML-3D predictions of the impact force show a better agreement with experimental data. Indeed, from $t^* > 15$, the HML-3D and NSTP-3D

10969837, 0, Downloaded from https://onlinelibrary.wiley.com/doi/10.1002/esp.5817 by Uni Federico Ii Di Napoli, Wiley Online Library on [20/03/2024]. See the Terms and Conditions (https://onlinelibrary.wiley.com/terms-and-conditions) on Wiley Online Library for rules of use; OA articles are governed by the applicable Creative Commons License

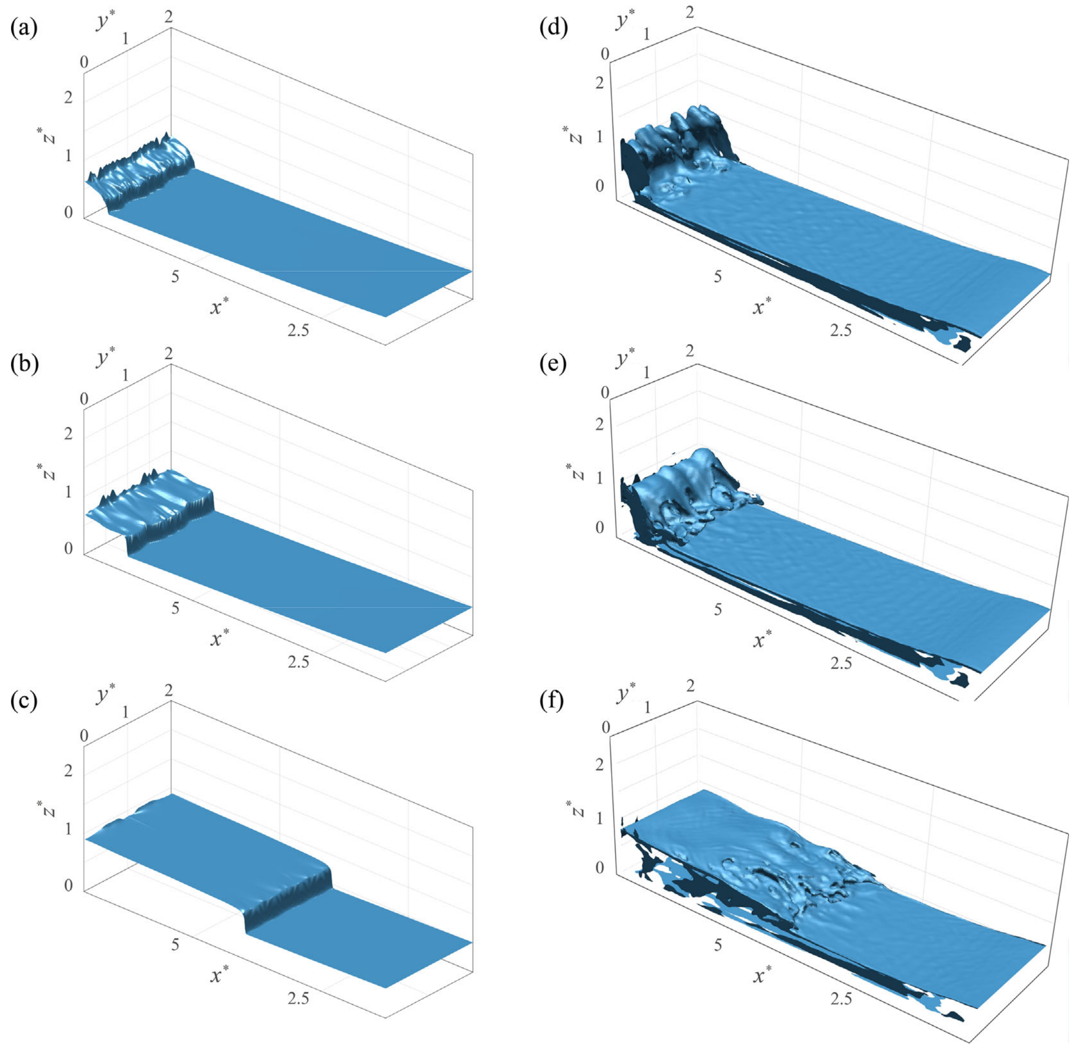

FIGURE 13 Water level predicted in the $h_0 = 0.2$ m case. (a–c) HML-3DL simulation; (d–f) NSTP-3D simulation. Results are shown for three nondimensional times (a,d) $t^* = 5.5$, (b,e) $t^* = 6.5$ and (c,f) $t^* = 10.5$. HML, hydrostatic multi-layer; NSTP, Navier–Stokes two-phase.

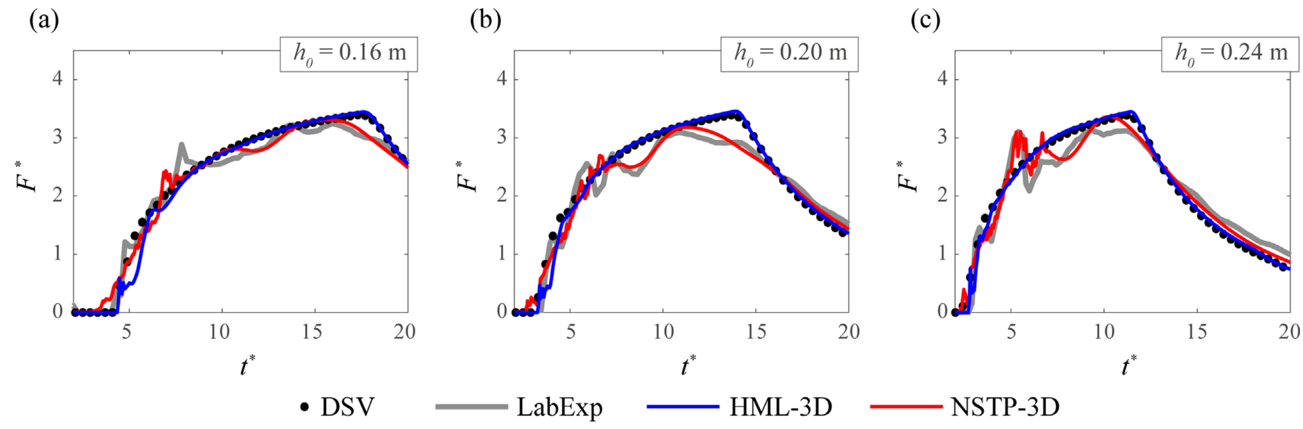

FIGURE 14 Evolution of the dimensionless impact forces (a) $h_0 = 0.16$ m, (b) $h0 = 0.2$ m and (c) $h_0 = 0.24$ m. The curves are based on laboratory experiments (grey thicker lines), DSV simulations (black dots), NSTP-3D simulations (red lines) and HML-3D simulations (blue lines). DSV, De Saint-Venant equation; HML, hydrostatic multi-layer; NSTP, Navier–Stokes two-phase.

predictions are virtually identical. Also, it is worth noting that the impact forces predicted by the simplest 1D-DSV model and by the HML-3D model are practically identical (see the dotted black line and the continuous blue line in Figure 14a–c). Both models overestimate by about 10% the peak impact force, which appears to be slightly delayed in time with respect to the experimental data.

5 | CONCLUSIONS

The experimental and numerical data presented in this paper support several conclusions. Hydrostatic models are able to fairly accurately reproduce the wave front celerity during the propagation phase and the reflection phase after the backward-propagating hydraulic jump is

10969837, 0, Downloaded from https://onlinelibrary.wiley.com/doi/10.1002/esp.5817 by Uni Federico Ii Di Napoli, Wiley Online Library on [20/03/2024]. See the Terms and Conditions (https://onlinelibrary.wiley.com/terms-and-conditions) on Wiley Online Library for rules of use; OA articles are governed by the applicable Creative Commons License

generated. Moreover, this type of models capture fairly accurately the peak force induced by the dam-break wave on the end wall, with an overestimation of the peak value of less than 10%.

Compared with the HML-3D simulations, the pressure and impact forces predicted by the corresponding 2D simulations, while sharing the same trends, showed irregular and high-frequency nonphysical oscillations. These fluctuations are most likely due to the suppression of vortex stretching along the spanwise direction.

The NSTP-2D model is computationally more expensive than the DSV and the HML-2D models; however, it does not predict the celerity of the wave front better than hydrostatic models. In particular, such 2D models overestimate the front celerity due to the overprediction of the water levels during the reflection phase.

The NSTP-2D model predicts fairly accurately the maximum impact force on the downstream wall and accurately reproduces the oscillations due to the formation of Favre waves. However, nonphysical oscillations occur in the solutions during the jet overturning.

Although a NSTP-3D model is considerably more computationally expensive compared with the other models, it is able to reproduce correctly the whole dynamics of the dam-break flow in terms of free-surface evolution, local pressure distribution and impact force induced on the downstream wall.

To sum up, a cost-benefit analysis shows that from an engineering point of view, hydrostatic models reproduce fairly well the general features of the dam-break flow. However, even if the flow could be considered two-dimensional from an engineering point of view, the adoption of a 2D approach to simulate such flows generates nonphysical oscillations in the time histories of the pressure and impact forces. This should limit their application to real problems where no detailed validation data are present as in such cases it is not always possible to distinguish between physical and nonphysical oscillations. The best predictions are given by the NSTP-3D model. Finally, if it is not practical to use such a 3D model, it could be more convenient to use the more simple DSV-1D model, which is able to predict fairly accurately the impact time and the peak value of the impact force on the end wall.

ACKNOWLEDGEMENTS

Giovanni La Forgia was partially supported by the project 'Solid transport in rivers and morphodynamic equilibrium of the coasts' (TRASFLUV), financed by Lazio Region, Italy.

AUTHOR CONTRIBUTIONS

Andrea Del Gaudio, Giovanni La Forgia, Cristiana Di Cristo, Angelo Leopardi, Michele Iervolino, Andrea Vacca: conceptualisation. Francesco De Paola and Angelo Leopardi: funding acquisition. Andrea Del Gaudio and Giovanni La Forgia: methodology. Andrea Del Gaudio and Giovanni La Forgia: investigation. Andrea Del Gaudio, Giovanni La Forgia, Cristiana Di Cristo and Andrea Vacca: resources. Cristiana Di Cristo, Angelo Leopardi, Michele Iervolino, Andrea Vacca: supervision. Andrea Del Gaudio, Giovanni La Forgia: writing-initial draft. George Constantinescu, Francesco De Paola, Cristiana Di Cristo, Angelo Leopardi, Michele Iervolino, Andrea Vacca: writing-reviewing and editing.

CONFLICT OF INTEREST STATEMENT

The authors declare no competing interests.

DATA AVAILABILITY STATEMENT

Data are available on request from the authors.

ORCID

Andrea Del Gaudio https://orcid.org/0000-0003-1419-1090
Giovanni La Forgia https://orcid.org/0000-0002-8543-6369
Cristiana Di Cristo https://orcid.org/0000-0001-6578-4502
Michele Iervolino https://orcid.org/0000-0001-8344-8334
Angelo Leopardi https://orcid.org/0000-0001-6314-0279

REFERENCES

Ai, C., Ma, Y., Ding, W., Xie, Z. & Dong, G. (2022) Three-dimensional non-hydrostatic model for dam-break flows. *Physics of Fluids*, 34(2), 22105.

Arnason, H. (2005) *Interactions between an incident bore and a free-standing coastal structure*. University of Washington.

Aureli, F., Dazzi, S., Maranzoni, A., Mignosa, P. & Vacondio, R. (2015) Experimental and numerical evaluation of the force due to the impact of a dam-break wave on a structure. *Advances in Water Resources*, 76, 29–42. Available from: https://www.sciencedirect.com/science/article/pii/S0309170814002292

Aureli, F., Maranzoni, A., Petaccia, G. & Soares-Frazão, S. (2023) Review of experimental investigations of dam-break flows over fixed bottom. *Water*, 15(6), 1229.

Bidoae, R., Ciobotaru, R.M. & Raad, P.E. (2003) Interaction of free surface flows with unrestrained solid-porous bodies, Fluids engineering division summer meeting, Vol. 36975.

Bigdeli, M., Taheri, M. & Mohammadian, A. (2023) Numerical modeling of dam-break flood flows for dry and wet sloped beds. *ISH Journal of Hydraulic Engineering*, 29(3), 259–269. Available from: https://doi.org/10.1080/09715010.2022.2052986

Biscarini, C., Di Francesco, S. & Manciola, P. (2010) CFD modelling approach for dam break flow studies. *Hydrology and Earth System Sciences*, 14(4), 705–718.

Bredmose, H., Hunt-Raby, A., Jayaratne, R. & Bullock, G.N. (2010) The ideal flip-through impact: experimental and numerical investigation. *Journal of Engineering Mathematics*, 67, 115–136.

Brufau, P., Vázquez-Cendón, M.E. & García-Navarro, P. (2002) A numerical model for the flooding and drying of irregular domains. *International Journal for Numerical Methods in Fluids*, 39(3), 247–275.

Burchard, H. & Baumert, H. (1995) On the performance of a mixed-layer model based on the $\kappa-\varepsilon$ turbulence closure. *Journal of Geophysical Research: Oceans* 100(C5): 8523–8540.

Castro-Orgaz, O. & Hager, W.H. (2019) *Shallow water hydraulics*. Springer Cham.

Chanson, H. (2009) Application of the method of characteristics to the dam break wave problem. *Journal of Hydraulic Research*, 47(1), 41–49.

Christensen, A., Twilley, R.R., Willson, C.S. & Castañeda-Moya, E. (2020) Simulating hydrological connectivity and water age within a coastal deltaic floodplain of the mississippi river delta. *Estuarine, Coastal and Shelf Science*, 245, 106995.

Constantinescu, G. (2014) LE of shallow mixing interfaces: A review. *Environmental Fluid Mechanics*, 14, 971–996. Available from: https://doi.org/10.1007/s10652-013-9303-6

Dai, S., He, Y., Yang, J., Ma, Y., Jin, S. & Liang, C. (2020) Numerical study of cascading dam-break characteristics using SWEs and RANS. *Water Supply*, 20(1), 348–360.

Dan, S., Walstra, D. J.R., Stive, M. J.F. & Panin, N. (2011) Processes controlling the development of a river mouth spit. *Marine Geology*, 280(1-4), 116–129.

Di Cristo, C., Greco, M., Iervolino, M. & Vacca, A. (2020) Interaction of a dam-break wave with an obstacle over an erodible floodplain. *Journal of Hydroinformatics*, 22(1), 5–19.

Di Cristo, C., Greco, M., Iervolino, M. & Vacca, A. (2021) Impact force of a geomorphic dam-break wave against an obstacle: effects of sediment inertia. *Water* 13.

10969837, 0, Downloaded from https://onlinelibrary.wiley.com/doi/10.1002/esp.5817 by Uni Federico Ii Di Napoli, Wiley Online Library on [20/03/2024]. See the Terms and Conditions (https://onlinelibrary.wiley.com/terms-and-conditions) on Wiley Online Library for rules of use; OA articles are governed by the applicable Creative Commons License

Fang, J., Cui, Y., Li, X. & Nie, J. (2022) A new insight into the dynamic impact between geophysical flow and rigid barrier. *Computers and Geotechnics*, 148, 104790.

Favre, H. (1935) Etude theorique et experimental des ondes de translation dans les canaux decouverts. *Dunod* 150.

Fluixá-Sanmartín, J., Altarejos-García, L., Morales-Torres, A. & Escuder-Bueno, I. (2018) Climate change impacts on dam safety. *Natural Hazards and Earth System Sciences*, 18(9), 2471–2488.

Garoosi, F., Mellado-Cusicahua, A.N., Shademani, M. & Shakibaeinia, A. (2022) Experimental and numerical investigations of dam break flow over dry and wet beds. *International Journal of Mechanical Sciences*, 215, 106946.

Gonzalez-Juez, E., Meiburg, E., Tokyay, T. & Constantinescu, G. (2010) Gravity current flow past a circular cylinder: forces, wall shear stresses and implications for scour. *Journal of Fluid Mechanics*, 649, 69–102.

Hattori, M., Arami, A. & Yui, T. (1994) Wave impact pressure on vertical walls under breaking waves of various types. *Coastal Engineering*, 22(1-2), 79–114.

Heikkila, J. & Silvén, O. (1997) A four-step camera calibration procedure with implicit image correction, Proceedings of ieee computer society conference on computer vision and pattern recognition, IEEE.

Hirt, C.W. & Nichols, B.D. (1981) Volume of fluid (VOF) method for the dynamics of free boundaries. *Journal of Computational Physics*, 39(1), 201–225.

Kamra, M.M., Mohd, N., Liu, C., Sueyoshi, M. & Hu, C. (2018) Numerical and experimental investigation of three-dimensionality in the dam-break flow against a vertical wall. *Journal of Hydrodynamics*, 30(4), 682–693.

Kleefsman, K. M.T., Fekken, G., Veldman, A. E.P., Iwanowski, B. & Buchner, B. (2005) A volume-of-fluid based simulation method for wave impact problems. *Journal of Computational Physics*, 206(1), 363–393.

Kocaman, S., Gúzel, H., Evangelista, S., Ozmen-Cagatay, H. & Viccione, G. (2020) Experimental and numerical analysis of a dam-break flow through different contraction geometries of the channel. *Water (Switzerland)* 12(4).

La Forgia, G., Cavaliere, D., Espa, S., Falcini, F. & Lacorata, G. (2022) Numerical and experimental analysis of lagrangian dispersion in two-dimensional chaotic flows. *Scientific Reports*, 12(1), 7461.

La Forgia, G., Tokyay, T., Adduce, C. & Constantinescu, G. (2018) Numerical investigation of breaking internal solitary waves. *Physical Review Fluids*, 3(10), 104801.

Lai, J.-S., Lin, G.-F. & Guo, W.-D. (2005) An upstream flux-splitting finite-volume scheme for 2D shallow water equations. *International Journal for Numerical Methods in Fluids*, 48(10), 1149–1174.

Lara, J.L., del Jesus, M. & Losada, I.J. (2012) Three-dimensional interaction of waves and porous coastal structures: Part II: experimental validation. *Coastal Engineering*, 64, 26–46.

Larocque, L.A., Imran, J. & Chaudhry, M.H. (2013) 3D numerical simulation of partial breach dam-break flow using the LES and $k-\epsilon$ turbulence models. *Journal of Hydraulic Research* 51(2): 145–157.

Lauber, G. & Hager, W.H. (1998) Experiments to dambreak wave: sloping channel. *Journal of Hydraulic Research*, 36(5), 761–773.

Lesser, G.R., van Kester, J. A. & Stelling, G.S. (2004) Development and validation of a three-dimensional morphological model. *Coastal Engineering*, 51(8-9), 883–915.

Ling, P., Ting, Z., Jianzhu, L. & Ping, F. (2023) Three-dimensional numerical study of dam-break flood impacting problem with VOF method and different turbulence closures. *Water Resources Management*. Available from: https://doi.org/10.1007/s11269-023-03530-z

Liu, J., Hayatdavoodi, M. & Ertekin, R.C. (2020) On bore dynamics and pressure: RANS Green-Naghdi, and Saint-Venant equations. *Journal of Offshore Mechanics and Arctic Engineering* 142(2).

Liu, S., Nistor, I., Mohammadian, A. & Azimi, A.H. (2022) Experimental investigation on the impact of dam-break induced surges on a vertical wall. *Fluids*, 7(8), 258.

Lobovsk, L., Botia-Vera, E., Castellana, F., Mas-Soler, J. & Souto-Iglesias, A. (2014) Experimental investigation of dynamic pressure loads during dam break. *Journal of Fluids and Structures*, 48, 407–434. Available from: https://www.sciencedirect.com/science/article/pii/S0889974614000656

Lynett, P.J. (2022) Tsunami inundation, modeling of. In: Tilling, R.I. (Ed.) *Complexity in tsunamis, volcanoes, and their hazards*. New York, NY: Springer US, 117–133. Available from: https://doi.org/10.1007/978-1-0716-1705-2_569

Marsooli, R. & Wu, W. (2014) 3-D finite-volume model of dam-break flow over uneven beds based on VOF method. *Advances in Water Resources*, 70, 104–117.

Mingham, C.G. & Causon, D.M. (1998) High-resolution finite-volume method for shallow water flows. *Journal of Hydraulic Engineering*, 124(6), 605–614.

Munoz, D.H. & Constantinescu, G. (2020) 3-D dam break flow simulations in simplified and complex domains. *Advances in Water Resources*, 137, 103510.

Nistor, I., Nouri, Y., Palermo, D. & Cornett, A. (2009) Experimental investigation of the impact of a tsunami-induced bore on structures. In *Coastal engineering 2008: (in 5 volumes)*, World Scientific; 3324–3336.

Oertel, M. & Bung, D.B. (2012) Initial stage of two-dimensional dam-break waves: laboratory versus VOF. *Journal of Hydraulic Research*, 50(1), 89–97.

Ortiz, P. (2014) Shallow water flows over flooding areas by a flux-corrected finite element method. *Journal of Hydraulic Research*, 52(2), 241–252.

Ozmen-Cagatay, H. & Kocaman, S. (2011) Dam-break flow in the presence of obstacle: experiment and CFD simulation. *Engineering Applications of Computational Fluid Mechanics*, 5(4), 541–552.

Patankar, S. (2018) *Numerical heat transfer and fluid flow*. Taylor & Francis.

Peregrine, D.H. (2003) Water-wave impact on walls. *Annual Review of Fluid Mechanics*, 35(1), 23–43.

Phillips, N.A. (1957) A coordinate system having some special advantages for numerical forecasting. *Journal of Meteorology*, 14, 184–185.

Ramsden, J.D. (1996) Forces on a vertical wall due to long waves, bores, and dry-bed surges. *Journal of Waterway, Port, Coastal, and Ocean Engineering*, 122(3), 134–141.

Robertson, I.N., Paczkowski, K., Riggs, H.R. & Mohamed, A. (2013) Experimental investigation of tsunami bore forces on vertical walls. *Journal of Offshore Mechanics and Arctic Engineering* 135(2).

Roelvink, J. A. T.M. & Banning, G. K. F. M.V. (1995) Design and development of DELFT3D and application to coastal morphodynamics. *Oceanographic Literature Review*, 11(42), 925.

Shen, J., Wei, L., Wu, D., Liu, H. & Huangfu, J. (2020) Spatiotemporal characteristics of the dam-break induced surge pressure on a vertical wall. *Coastal Engineering Journal*, 62(4), 566–581.

Simsek, O. & Islek, H. (2023) 2D and 3D numerical simulations of dam-break flow problem with RANS, DES, and LES. *Ocean Engineering*, 276, 114298. Available from: https://www.sciencedirect.com/science/article/pii/S0029801823006820

Soares Frazao, S. & Zech, Y. (2002) Dam break in channels with 90 degrees bend. *Journal of Hydraulic Engineering*, 128(11), 956.

Stamataki, I., Zang, J., Buldakov, E., Kjeldsen, T. & Stagonas, D. (2018) Study of dam break flow interaction with urban settlements over a sloping channel, E3s web of conferences, Vol. 40, E3S Web of Conferences.

Tan, T., Ma, Y., Zhang, J., Niu, X. & Chang, K.-A. (2023) Experimental study on flow kinematics of dam-break induced surge impacting onto a vertical wall. *Physics of Fluids* 35(2).

The MathWorks Inc. (2022) MATLAB version: 9.13.0 (R2022b), Natick, Massachusetts, United States. Available from: https://www.mathworks.com

Tokyay, T. & Constantinescu, G. (2015) The effects of a submerged non-erodible triangular obstacle on bottom propagating gravity currents. *Physics of Fluids* 27(5).

Tokyay, T., Constantinescu, G. & Meiburg, E. (2011) Lock-exchange gravity currents with a high volume of release propagating over a periodic array of obstacles. *Journal of Fluid Mechanics*, 672, 570–605.

Tokyay, T., Constantinescu, G. & Meiburg, E. (2012) Tail structure and bed friction velocity distribution of gravity currents propagating over an array of obstacles. *Journal of Fluid Mechanics*, 694, 252–291.

10969837, 0, Downloaded from https://onlinelibrary.wiley.com/doi/10.1002/esp.5817 by Uni Federico Ii Di Napoli, Wiley Online Library on [20/03/2024]. See the Terms and Conditions (https://onlinelibrary.wiley.com/terms-and-conditions) on Wiley Online Library for rules of use; OA articles are governed by the applicable Creative Commons License

Tokyay, T., Constantinescu, G. &Meiburg, E. (2014) Lock exchange gravity currents with a low volume of release propagating over an array of obstacles. *Journal of Geophysical Research: Oceans*, 119(5), 2752–2768. Available from: https://doi.org/10.1002/2013JC009721

Wüthrich, D., Pfister, M., Nistor, I. & Schleiss, A.J. (2018) Experimental study on forces exerted on buildings with openings due to extreme hydrodynamic events. *Coastal Engineering*, 140, 72–86.

Wang, S., Garlock, M., Deike, L. & Glisic, B. (2022) Feasibility of kinetic umbrellas as deployable flood barriers during landfalling hurricanes. *Journal of Structural Engineering*, 148(5), 4022047.

Wilcox, D. (1998) *Turbulence modeling for CFD*. DCWI industries, Inc. La Canada, California.

Wúthrich, D., Pfister, M. & Schleiss, A.J. (2019) Effect of bed roughness on tsunami-like waves and induced loads on buildings. *Coastal Engineering*, 152, 103508. Available from: https://www.sciencedirect.com/science/article/pii/S0378383918306008

Xie, W. & Shimozono, T. (2022) Water surge impingement onto a vertical wall: laboratory experiments and stochastic analysis on impact pressure. *Ocean Engineering*, 248, 110422.

Xu, W.L., Chen, H.Y., Xue, Y. & Niu, Z.P. (2013) *The chain of dam break in cascade reservoirs*. Beijing (in Chinese): China Water & Power Press.

Yang, S., Yang, W., Qin, S. & Li, Q. (2019) Comparative study on calculation methods of dam-break wave. *Journal of Hydraulic Research*, 57(5), 702–714.

Zh, Z. (2000) A flexible new technique for camera calibration. *IEEE Transactions on Pattern Analysis and Machine Intelligence*, 22(11), 1330–1334.

How to cite this article: Del Gaudio, A., La Forgia, G., Constantinescu, G., De Paola, F., Di Cristo, C., Iervolino, M. et al. (2024) Modelling the impact of a dam-break wave on a vertical wall. *Earth Surface Processes and Landforms*, 1–16. Available from: https://doi.org/10.1002/esp.5817

10969837, 0, Downloaded from https://onlinelibrary.wiley.com/doi/10.1002/esp.5817 by Uni Federico Ii Di Napoli, Wiley Online Library on [20/03/2024]. See the Terms and Conditions (https://onlinelibrary.wiley.com/terms-and-conditions) on Wiley Online Library for rules of use; OA articles are governed by the applicable Creative Commons License